JOURNAL OF SPACECRAFT AND ROCKETS
Vol. 46, No. 6, November–December 2009

Shock/Boundary-Layer Interaction Effects on Transverse Jets in Crossflow over a Flat Plate

Dean A. Dickmann*
Lockheed Martin Missiles and Fire Control, Grand Prairie, Texas 75265
and
Frank K. Lu†
University of Texas at Arlington, Arlington, Texas 76019

DOI: 10.2514/1.39297

This study examines the near-field mean flow structure of a transverse jet in subsonic and supersonic crossflows using computational fluid dynamics. The results show the shock/boundary-layer interaction present in supersonic crossflow alters the mean flow in the near field of a transverse jet compared to subsonic crossflow. The interaction bifurcates the phase portrait of the separation topology through the addition of saddle points, nodes, and separation lines. In subsonic crossflow at a nozzle pressure ratio of 5, the near-field, mean flow structure includes horn vortices, near-field wake vortices, and far-field wake vortices. In supersonic crossflow, at the same pressure ratio, the bifurcation resulting from the shock/boundary-layer interaction eliminates the near-field and far-field wake vortices leaving only the horn vortices. The shock/boundary-layer interaction also generated another set of global separation lines within which a set of horseshoe vortices formed. These global separation lines did not converge, allowing the horseshoe vortices to affect the mean flow along the entire length of the plate downstream of the jet. Alteration of the mean flow in the near field affected the surface pressure distribution and ultimately the jet interaction performance coefficients.

Nomenclature

$\bar{C}_f$	=	transformed skin friction coefficient
C_m	=	pitching moment coefficient
C_N	=	normal force coefficient
C_T	=	thrust coefficient, $F/(q_\infty S_{\text{ref}})$
d	=	diameter, ft
l, L	=	length, ft
M	=	freestream Mach number
PR	=	pressure ratio
p	=	pressure, psf
$\overline{Re}_\theta$	=	transformed Reynolds number
T	=	temperature, R
x	=	streamwise Cartesian coordinate, ft
y	=	normal direction, ft
z	=	spanwise direction, ft
ε	=	amplification coefficient

Subscripts

jet	=	jet exit
ji	=	jet interaction
LE	=	leading edge
noz	=	nozzle centerline
ref	=	reference
t	=	total
x	=	x direction

Presented as Paper 3723 at the 38th Fluid Dynamics Conference and Exhibit, Seattle, WA, 23–26 June 2008; received 24 June 2008; revision received 4 September 2009; accepted for publication 4 September 2009.

*Senior Staff Engineer, Systems Engineering Department.

†Professor and Director, Aerodynamics Research Center, Mechanical and Aerospace Engineering Department, Box 19018. Associate Fellow AIAA.

I. Introduction

JETS issuing perpendicularly to a freestream have been the subject of research for more than 60 years [1]. Much of the research has been focused on vertical/short takeoff and landing applications, where the freestream is either quiescent or regarded as incompressible, or scramjet engine applications where mixing is the primary concern. Reaction jet control systems (RJCS) have received less attention, but have gained focus recently as vehicle maneuverability requirements have increased. The interest in RJCS applications is directed at the surface pressure perturbations caused by the interaction between the jet and freestream, generally referred to as jet interaction (JI), which can alter the effectiveness of the RJCS. Ferrari [2], Spaid [3], and Spaid and Cassel [4] have suggested a transverse jet can be represented by a solid body of given length and shape in inviscid flow. Observations have revealed this simplistic model is not realistic because it does not include plume overexpansion, proper vortex generation, or the proper separation topology. Current understanding of the near-field mean flow structure in a supersonic freestream due to Morkovin et al. [5], Cubbison et al. [6], Fric and Roshko [7], and Roger and Chan [8] has been described and illustrated by Champigny and Lacau [9]. This mean flow structure has been confirmed by Gruber et al. [10] and is widely accepted among most researchers.

The mean flow structure depicted by Champigny and Lacau [9] is shown in Fig. 1. Among the features of this model is the λ-shock structure upstream of the jet created by the interaction between the bow shock and approaching boundary layer, the subsequent three-dimensional separation zone wrapping around the jet, and the counter-rotating jet vortices. In addition to these features, a barrel shock around the plume terminating in a Mach disk, horseshoe vortices convecting around the jet, and a downstream secondary shock are present. The current study seeks to verify these flow structures via numerical calculation, to examine the complex separation topology of JI, and to identify amplification effects on the jet thrust.

The significance of this investigation lies in the identification of flow structure present in both subsonic and supersonic crossflows overlooked by previous studies of the near-field mean flow structure. Identification of this flow structure provides a better understanding of the mechanisms causing the surface pressure perturbations affecting the performance of RJCS.

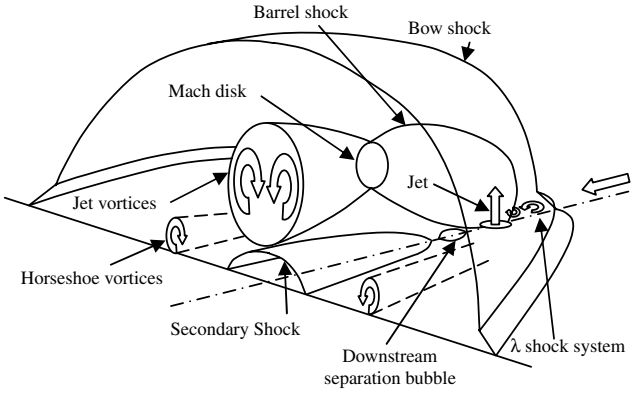

Fig. 1 Currently accepted near-field mean flow structure.

The three-dimensional viscous-inviscid interaction present in JI flowfields precludes the use of many simplifying assumptions typically used in the previous analyses, and so a three-dimensional Reynolds-averaged Navier–Stokes (N-S) solver was used to simulate the interaction. Two solvers were evaluated, namely, Falcon [11], a Lockheed Martin code, and GASP [11], a commercially available code maintained by Aerosoft, to determine the ability of each to properly simulate the near-field mean flow structure. The evaluation concluded Falcon with a *k-kl* turbulence model [12] was the more appropriate numerical model. The primary reason Falcon was judged the more appropriate model was its ability to more accurately predict undisturbed turbulent boundary-layer profiles over a flat plate in supersonic flow.

II. Preliminary Flow Simulations

Falcon, a 3-D full Navier–Stokes finite volume solver developed by Lockheed Martin, was validated with the Smith κ-$\kappa\ell$ turbulence model [12] against pressure data from a test of Mach 2.61 flow over a flat plate with a jet conducted by Dowdy and Newton [13] and several cases of flow over a flat plate. The κ-$\kappa\ell$ model is a two-equation model using an equation for the turbulent kinetic energy and another for the product of turbulent kinetic energy and the turbulent length scale. Falcon solves the full set of the unsteady three-dimensional, Reynolds-averaged conservation equations [14]. The time derivatives are discretized by first-order forward difference operators while the viscous terms are discretized by second-order central difference operators. Cell volume properties are distributed to the cell face using the Monotonic Upstream-centered Scheme for Conservative Laws (MUSCL) due to Van Leer [15]. To reduce numerical oscillations, the fluxes at each cell face are then split into two parts to reflect the dependence domains according to characteristic theory using the flux-difference splitting method of Roe [16] with the SUPERBEE flux limiter [17]. The discretized equations were solved using Stone's strongly implicit procedure [18]. A steady-state solution is determined by examination of convergence criteria.

A. Convergence Criteria

Falcon solves a finite difference approximation of the nondimensional unsteady N-S equations given an initial condition until a steady-state solution is reached. Ideally, the time-dependent terms in the approximated equations would be exactly zero when the steady-state solution is reached. However, in general, a solution can be deemed steady when the time-dependent terms are considered negligible compared to the other terms in the equations. Falcon computes the difference in the magnitude of the time-dependent terms from iteration n to $n+1$ for each grid cell. Summing the differences for each cell and dividing by the number of grid cells gives an estimate of the magnitude of the time-dependent terms relative to the other terms in the equations. The result of this summation is referred to as the residual. This is one of the criteria used in this study to determine if a solution has reached steady state. The other criteria were the integrated surface forces computed by Falcon. If the residual drops 3 orders of magnitude and the surface forces vary less than 5% over 1000 iterations, the solution is considered steady state. The normalized residual and integrated surface force histories for the Mach 2.0 flat plate simulation are shown in Fig. 2 as an example of the criterion used to determine a steady-state solution.

Figure 2a shows the residual plotted against iteration on a semilog plot. The residual oscillates while the solution converges, but, in general, decreases in a fairly logarithmic manner. Figure 2b shows the components of the integrated surface forces vary randomly with iteration, settling to steady-state values. When the convergence criteria for both the normalized residual and the integrated surface forces are met, the solution is considered steady state and the simulation halted.

B. Grid Resolution Study

The accuracy of a steady-state solution from any CFD solver is directly affected by the density of the grid. The grid density determines the accuracy of the information passed between cells from iteration to iteration. In this study, a relatively coarse grid and a relatively fine grid were exercised with Falcon to ensure grid density did not affect the computational results. If the results between grids do not change, the solutions are grid converged and there is a reasonable amount of confidence the grid will provide accurate results. A $403 \times 45 \times 133$ grid was used for the flow over the plate whereas a $17 \times 31 \times 7$ grid was used for the nozzle in the transverse jets in supersonic freestreams (TJISF) Falcon simulations. Figure 3a shows velocity vectors and pressure contours in the area of the barrel shock from the steady-state solution of the Mach 2 Falcon TJISF simulation for this grid. The barrel shock is smeared by the coarseness of the grid in the direction normal to the plate. The distribution in the axial direction appears to satisfactorily resolve the flow structure without smearing. Points were added in the normal direction to create a $403 \times 63 \times 133$ grid. This grid was applied the same flow conditions and the solution is shown in Fig. 3b.

A comparison of Figs. 3a and 3b shows that the finer grid satisfactorily resolved the barrel shock and Mach disk. Although this is evidence that a finer grid will resolve shocks, it is more important to

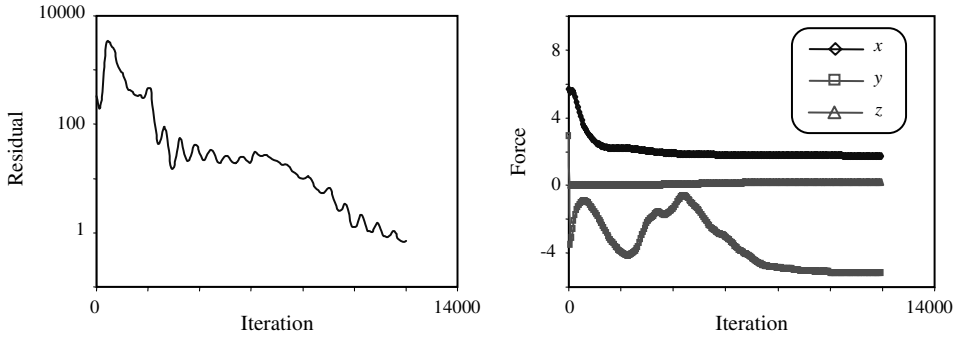

a) Residual **b) Force**

Fig. 2 Convergence criteria history, $M = 2.0$, $PR = 2000$.

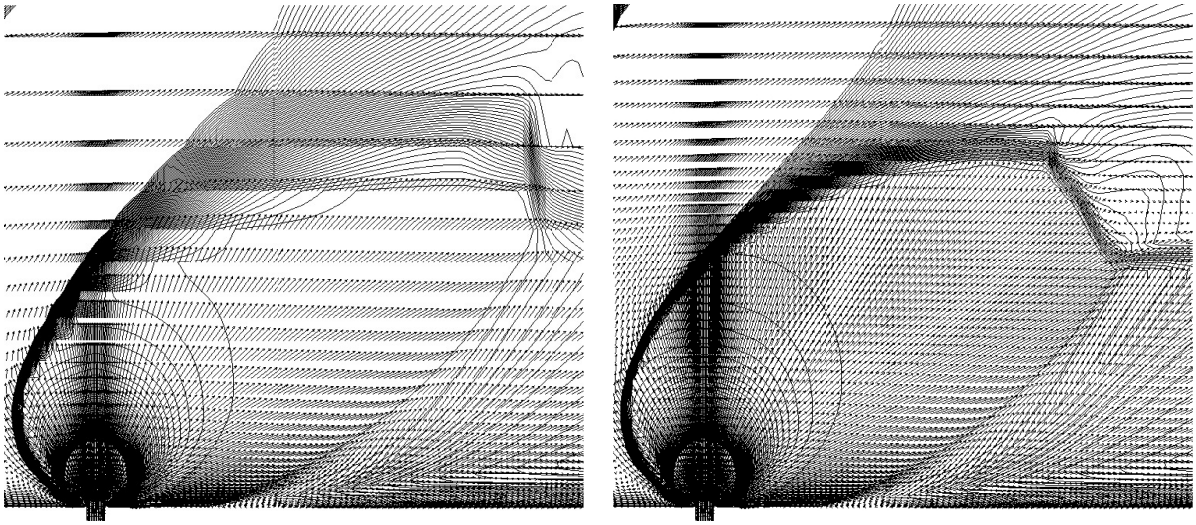

a) 403x45x133 b) 403x63x133

Fig. 3 Velocity vectors and pressure contours, $M = 2.0$, $PR = 2000$.

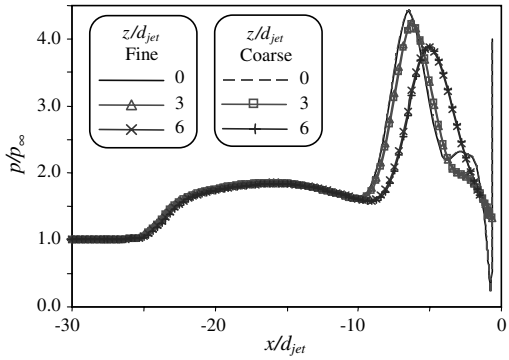

Fig. 4 Centerline pressure distributions, fine and coarse grids.

properly predict the pressure distribution so that the calculated forces and amplification coefficients are accurate. The pressure distributions at three transverse locations for both grid densities are compared in Fig. 4. These distributions were integrated and the force and amplification coefficients are given in Table 1.

The steady-state solutions from the fine and coarse grids are within 4% of each other. The excellent agreement indicates that the range of grid densities has an insignificant effect on the pressures and forces computed by Falcon.

In the next section, a limited validation of the code pertinent to the present study is provided. Computational results are compared to experimental boundary-layer data for undisturbed supersonic turbulent flow over a flat plate as well as surface pressure data for a flat plate with a transverse jet of pressure ratio 308 issuing normal to the freestream. Further validation for a large variety of flows can be found in [12].

C. Undisturbed Turbulent Boundary Layer

Falcon was applied to turbulent flow over a flat plate at Mach 2.23 and 4.5. The results are compared against the data of Shutts et al. [19] and Mabey et al. [20] as compiled by Fernholz and Finley [21] in Figs. 5 and 6. Figures 5 and 6 show the boundary-layer velocity profiles in wall coordinates [22] at two locations along the plate for the calculations, the experimental data, and the law-of-the-wall profiles [23].

The computed results matched the experimental and law-of-the-wall data well at both Mach 2.23 and 4.5 in the logarithmic and wake regions. Local skin friction coefficients are compared in Fig. 7. Hopkins and Inouye [24] recommended the Van Driest II transformation of the skin friction coefficient as the best possible method for transforming turbulent compressible flow to the incompressible plane for comparison with the Karman–Schoenherr (K-S) equation [Eq. (3) in [24]]. Figure 7 plots the transformed test data, the transformed computational results, and the K-S equation. The computational results compared well with test data and the K-S equation at Mach 2.23 but showed some discrepancy from both at Mach 4.5.

Table 1 Force and amplification coefficients for grid density

Grid	$C_{N\text{ji}}$	$C_{m\text{ji}}$	C_T	ε_N	ε_m
Coarse	−0.00847	0.00285	0.0184	1.461	1.063
Fine	−0.00817	0.00297	0.0184	1.461	1.029

D. Transverse Jet in Supersonic Crossflow with a Turbulent Boundary Layer

This section presents computational results compared to experimental data from Dowdy and Newton [13]. Dowdy and Newton collected a significant amount of surface pressure data on jets issuing from flat plates into supersonic crossflows. Falcon was applied to the test conditions listed in Table 2.

The resulting pressure distributions upstream and downstream of the jet along the centerline of the plate are compared with data from Dowdy and Newton [13] in Fig. 8. In Fig. 8, the pressure is normalized by the ambient pressure while the distance along the plate is normalized by the diameter of the jet d_{jet}, with the upstream distribution shown in Fig. 8a and the downstream shown in Fig. 8b. The diamond symbols represent the experimental data [13] and show the upstream pressure calculations agreed well with experimental data.

The experimental data in Fig. 8b show a massive overexpansion of the highly underexpanded jet ($PR = 308$) to below 10% of ambient. The overexpansion is followed by a gradual recompression until the pressure overshoots ambient before expanding back to ambient. The computations captured the overexpansion, but overpredicted the slope of the recompression and underpredicted the overshoot. Nonetheless, Fig. 8 shows the computations can provide reasonable results for transverse jets in a supersonic freestream.

III. Results and Discussion

A. Transverse Jet in Subsonic Crossflow

The study of transverse jets in a subsonic freestream is relevant to the study of transverse jets in supersonic freestreams because the counter-rotating vortices, a major feature of the flow structure in TJISF, are attributed to studies of transverse jets in subsonic

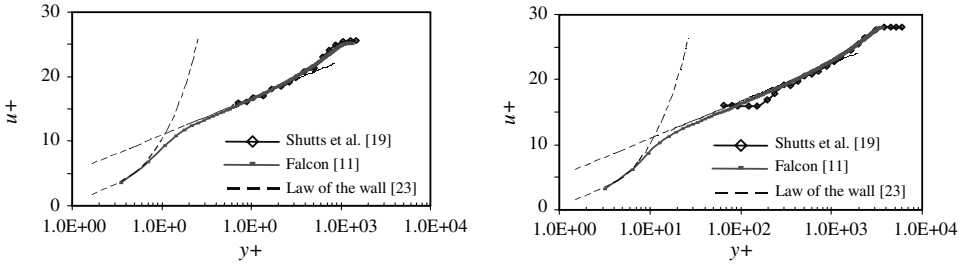

a) $x = 0.193$ m b) $x = 0.802$ m

Fig. 5 Comparison with Shutts et al.'s data [19] at $M = 2.23$, $Re_x = 25 \times 10^6$/m.

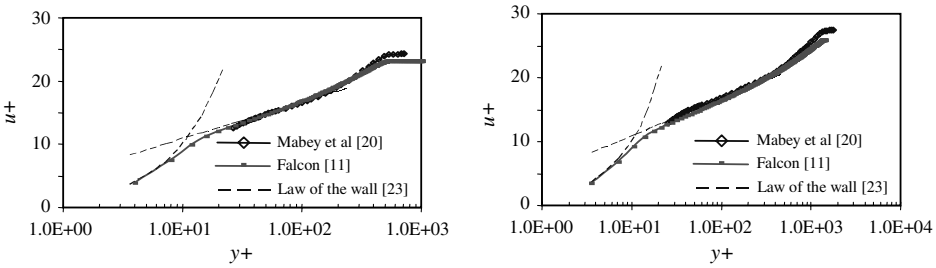

a) $x = 0.368$ m b) $x = 1.384$ m

Fig. 6 Comparison with Mabey et al.'s [20] data at $M = 4.5$, $Re_x = 28.1 \times 10^6$/m.

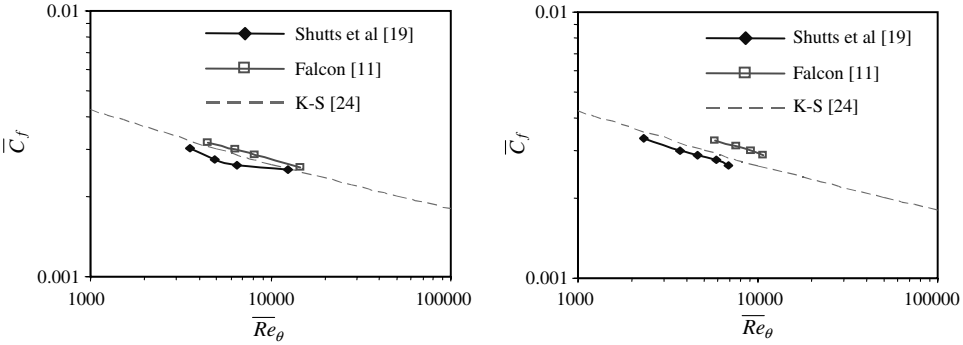

a) Mach 2.23 b) Mach 4.5

Fig. 7 Local skin friction coefficient.

freestreams. Proper prediction of these vortices in subsonic flow indicates the solver will be able to predict them in supersonic flow. Furthermore, it provides good background to contrast against TJISF.

A 457.2 mm square flat plate with a jet orifice located on the centerline, 177.8 mm from the leading edge, was analyzed with the coordinate system shown in Fig. 9. The jet issued from the convergent nozzle shown in Fig. 10 (dimensions are in millimeters).

The total pressure at the inlet of the nozzle was 327.8 kPa (6845.3 psf). The jet issued into a $M = 0.3$ freestream with an ambient pressure of 65.6 Pa (1369.1 psf) yielding a $PR = 5$. Surface pressure distributions upstream of the jet from the computations are shown in Fig. 11.

Figure 11 shows the normalized surface pressure plotted against the normalized axial distance in front of the jet at various lateral locations. The PR 5 jet resulted in supersonic flow at the exit plane of the nozzle with expansion waves emanating from the exit reducing the pressure within the jet as it expanded into the freestream. The expansion waves resulted in a favorable pressure gradient for the approaching boundary layer at lateral distances greater than 0.6 diameters. At lateral distances less than that, the jet obstruction caused the surface pressures to rise, creating an adverse pressure gradient immediately ahead of the jet expansion.

These pressure gradients near the jet affected the boundary-layer thickness in the near field as shown in Fig. 12. The boundary layer was 1 jet diameter thick upstream of the jet but, as it approached the jet, at lateral distances greater than 0.6 of a diameter, it became thinner because of the favorable pressure gradient. Near the centerline, the adverse pressure gradient caused a rapid thickening of the boundary layer with a corresponding decrease in surface shear stress. Because surface shear stresses tended toward zero, it was prudent to exam the skin friction lines, shown in Fig. 13, for evidence of flow separation.

Figure 13 shows skin friction lines on the surface of the flat plate in the near field of the jet with surface pressure contours shown in white. Determination of three-dimensional separation takes a different approach than two-dimensional separation [25–28]. Three-dimensional separation is described through a topology of saddle points, nodes, foci, streamlines, and separation lines. A line of separation is a particular skin friction line on which other skin friction lines converge. If the skin friction line on which others converge emanates

Table 2 Dowdy and Newton [13] test conditions

M	p_{tjet}, psf	T_{tjet}, R	p_∞, psf	$T_{t\infty}$, R	d_{jet}, in.	L_{plate}, in.	W_{plate}, in.
2.61	43,214.4	533.67	140.54	564.67	0.1	18	7.5

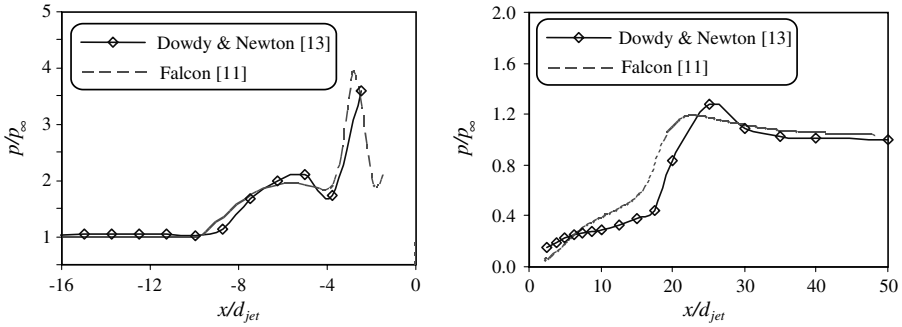

a) Upstream pressure distribution **b) Downstream pressure distribution**

Fig. 8 Upstream pressure distribution comparison.

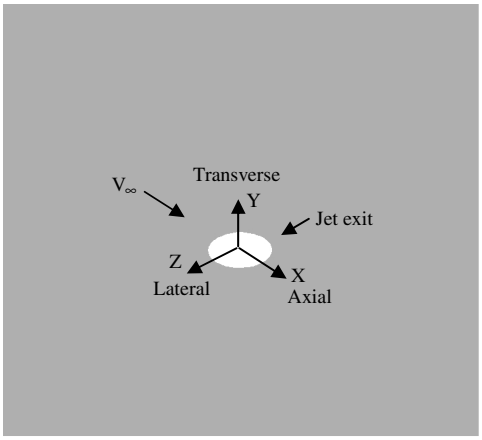

Fig. 9 Flat plate coordinate system.

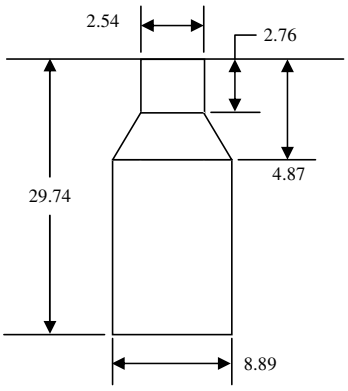

Fig. 10 Convergent nozzle configuration (dimensions in millimeters).

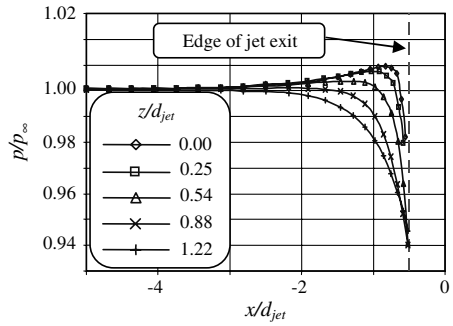

Fig. 11 Axial surface pressure, $M = 0.3$.

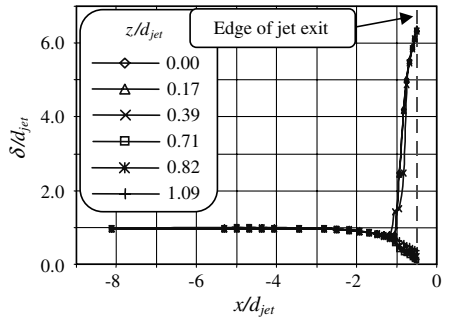

Fig. 12 Boundary-layer thickness, $M = 0.3$.

from a saddle point, it is said to be a global line of separation. Otherwise, it is a local line of separation. The convergence of the skin friction lines is the necessary condition for separation of a three-dimensional boundary layer. Furthermore, skin friction topologies with three-dimensional boundary-layer separation adhere to certain topological rules [26]. However, topological rules for a body in the presence of two streams are not well understood, and so the approach taken here was to identify the singularities on the surface, then identify the body type simulated by the interacting streams according to the topological rules for three-dimensional separation [26].

Figure 13 shows two saddle points, one upstream and one downstream at the plate/jet junction, and two separation foci at the plate/jet junction. Away from the plate/jet junction, downstream of the jet, there were two saddle points and one attachment node for a total of four saddle points and three nodes and foci. In addition to the saddle points, nodes, and foci, two pair of global separation lines, one

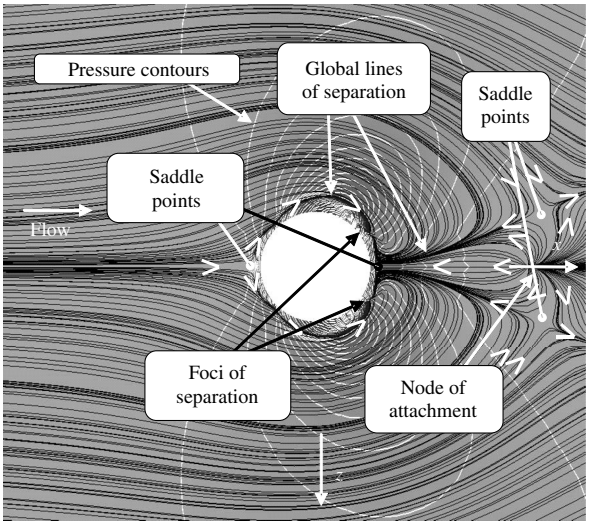

Fig. 13 Skin friction lines, $M = 0.3$.

around the jet and one downstream of the jet, are shown in Fig. 13. These topological features define the phase portrait of this flowfield and show that three-dimensional separation occurred around and downstream of the jet. This flow can be classified topologically as that of a two-dimensional plane cutting a three-dimensional body [26]. Such a classification is not surprising because the jet appears to the oncoming flow as a cylinder of finite height (a configuration proposed in early models of JI).

The global separation lines around the jet emanated from the upstream saddle point, wound into the separation foci, and were the base of the dividing surfaces [26] coiling into horn vortices, as shown in Fig. 14. Three-dimensional vorticity production through stretching and baroclinic interaction of pressure and density gradients, as well as two-dimensional vorticity production due to viscous effects and strain, generated these vortices. Vorticity production due to dilatation was negligible at this Mach number.

Figure 14 shows streamlines beginning just inside the jet exit and freestream streamlines just outside the jet exit. The streamlines just outside the jet exit follow the dividing surfaces emanating from the global separation lines on either side of the jet to form horn vortices, with the jet streamlines rotating into the horn vortices as both sets of streamlines convect downstream.

The global separation lines downstream of these horn vortices generated near-field and far-field wake vortices [11] as shown in Figs. 15 and 16. Figure 15 shows streamlines (arrows indicate the streamline path) following the dividing surfaces emanating from the downstream global separation lines between the saddle points and separation foci with skin friction lines (black). The streamlines show the near-field vortex pair convected upstream toward the jet with the left running vortex rotating clockwise and the right running vortex rotating counterclockwise.

Downstream of the saddle points, the dividing surfaces convected downstream away from the jet as shown in Fig. 16. These dividing surfaces coiled up into the far-field wake vortices with the left running vortex rotating clockwise and the right running vortex rotating counterclockwise.

This topology and associated flow structure are manifested in perturbations to the surface pressures near the jet. The region encompassing these perturbations defines the near field. Using the upstream half-saddle point, the two downstream saddle points, and the judicious selection of a pressure contour, a vast majority of the perturbations were captured and the near-field boundary was defined as shown in Fig. 17.

Figure 17 shows the near-field boundary with skin friction lines in black and surface pressure contours in white. The region outside this boundary had an insignificant effect on the JI force and moment while within this boundary the surface pressure perturbations dictated the JI force and moment. The two-lobe character of this

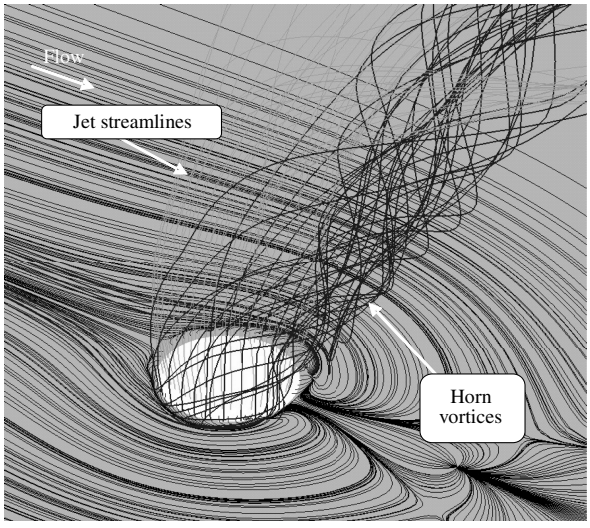

Fig. 14 Jet/near-jet streamlines, $M = 0.3$.

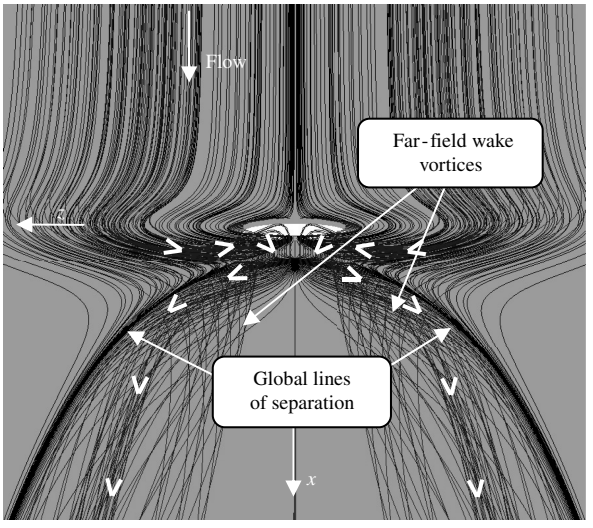

Fig. 16 Far-field wake vortices.

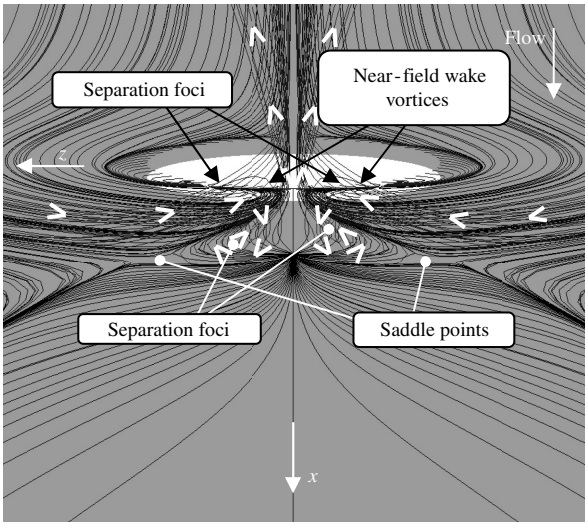

Fig. 15 Near-field wake vortices.

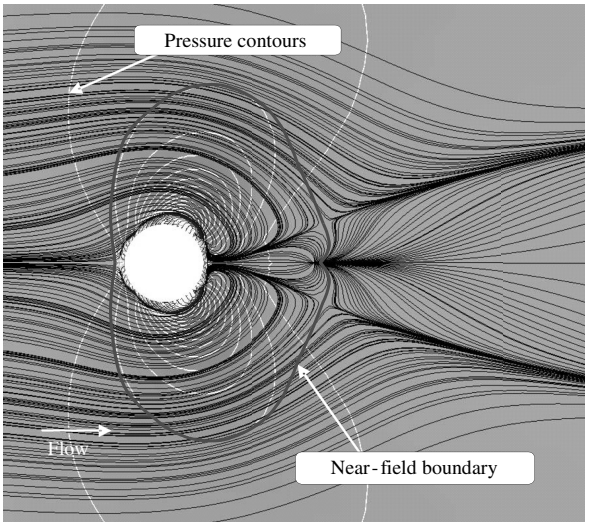

Fig. 17 Near-field boundary, $M = 0.3$.

region is interesting to note because, in the next section, when supersonic freestreams are considered, this character will be quite different.

The flow structure responsible for the modification of the surface pressures in the near field were the three-dimensional separation zone around the jet, the separation zone behind the jet, the horn and near-field wake vortices, as well as the attachment nodes, separation foci, and saddle points. The extent of the influence of these separation zones and topological features on the surface pressures and jet thrust were quantified by calculating the amplification coefficients. The amplification coefficients are defined as

$$\varepsilon_N = \frac{C_T + C_{N\text{ji}}}{C_T} \tag{1}$$

$$\varepsilon_m = \frac{C_T \frac{l_{\text{noz}}}{L_{\text{ref}}} + C_{m\text{ji}_{\text{LE}}}}{C_T \frac{l_{\text{noz}}}{L_{\text{ref}}}} \tag{2}$$

where

$$C_{N\text{ji}} = C_{N_{\text{JetOn}}} - C_{N_{\text{JetOff}}} - C_T \tag{3}$$

$$C_{m\text{ji}} = C_{m_{\text{JetOn}}} - C_{m_{\text{JetOff}}} - C_T \frac{l_{\text{noz}}}{L_{\text{ref}}} \tag{4}$$

Table 3 shows the thrust, force, and moment coefficients along with the amplification coefficients.

Amplification coefficients less than 1.0 indicate that the JI force opposed the force of the jet (i.e., attenuation) whereas amplification coefficients greater than 1.0 indicate that the JI force aided the force of the jet (i.e., amplification). Amplifications coefficients less than 0.0 indicate the direction of the jet thrust had been overwhelmed by JI forces and the resultant opposed the direction of the jet force. For the conditions of this simulation, the normal force amplification coefficient ε_N was +0.06 indicating the jet thrust was attenuated nearly 95%. The pitching moment amplification coefficient ε_m, taken about the leading edge of the plate, was −0.22 indicating the direction of the moment from the jet force was reversed and the magnitude attenuated almost 80%. This overwhelming impact on jet thrust performance shows how important JI forces and moments are to the operation of reaction jet control systems and how critical it is to understand the flow structure in the near field of the jet. In the following section, JI, surface pressures, and flow structure in a supersonic freestream are examined.

Table 3 Coefficients for subsonic freestream

M	PR	$C_{N\text{ji}}$	$C_{m\text{ji}}$	C_T	ε_N	ε_m
0.3	5.0	+1.54e − 3	+7.79e − 4	−1.64e − 3	+0.06	−0.22

B. Transverse Jet in Supersonic Crossflow

The flow structure in the near field of a transverse jet is very different in supersonic flow. In this section, a transverse jet with pressure ratio 5.0 issuing into a Mach 2 freestream is compared with the subsonic results of the previous section.

To maintain the same Reynolds number and jet pressure ratio at Mach 2, the ambient pressure was decreased to 9.83 kPa (205.4 psf) and the nozzle inlet total pressure was decreased to 49.16 kPa (1026.8 psf). Figure 18a shows the velocity vectors and pressure contours on the center plane of the flow domain upstream of the jet.

The underexpanded jet emerged from the nozzle, in the bottom right corner of Fig. 18a, obstructing the freestream approaching from the left. The obstruction deflected the supersonic freestream in the transverse and lateral directions generating a three-dimensional shock wave, typically referred to as the bow shock. The bow shock interacted with the approaching boundary layer to create a complex inviscid/viscous interaction known as a shock/boundary-layer interaction with a λ-shock structure [29]. As the bow shock intersected the boundary layer, the boundary layer sensed the pressure rise across the shock altering the viscous velocity profile and thickening the boundary layer as shown in Fig. 18b.

As the shock penetrated the boundary layer, it refracted downstream due to the change in the Mach number through the boundary layer. The refracted shock turned a portion of the boundary-layer flow toward the surface creating a node of attachment (or stagnation point) and an adverse pressure gradient that separated the boundary layer from the surface upstream of the node and created the upstream saddle point. As will be shown later, this saddle point originated a pair of separation lines and a separation zone between the freestream and the jet. Within the separation zone, the node of attachment shown in Fig. 18b divided two recirculation regions. The flow to the left of the node turned into an upstream recirculation between the upstream saddle point and node. The flow to the right turned toward the jet, deflected immediately upward into a saddle point within the interior of the flow, then turned back toward the attachment node.

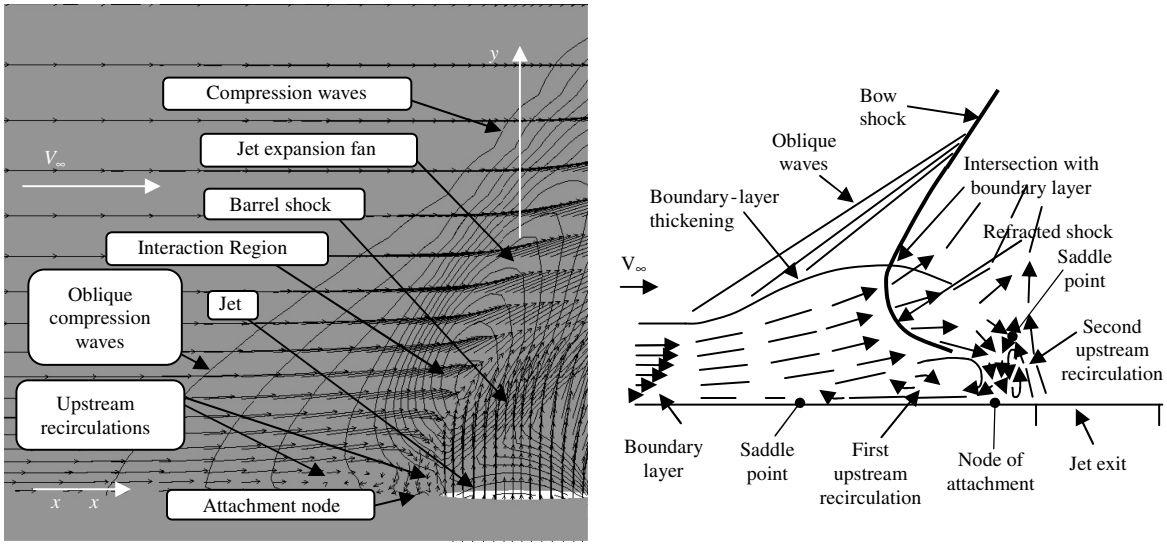

a) Pressure contours and in-plane velocity vectors **b) Sketch of interactions**

Fig. 18 Upstream pressure contours and velocity vectors, $M = 2.0$.

Outside the recirculation regions, upstream of the saddle point, the thickened boundary layer produced oblique compression waves which coalesced into the bow shock, creating the upstream leg of the λ. The refracted bow shock completed the λ-shock structure which dominated the near-field flow structure upstream of the jet and dramatically impacted the jet trajectory.

The strength of the λ shock bent the jet approximately 30° downstream. As the jet was turned, an oblique shock wave formed within the jet, typically referred to as the barrel shock, which propagated across the jet as illustrated in Fig. 19. As the barrel shock traveled across the jet, expansion waves emanating from the leeward edge of the jet exit intersected the barrel shock bending it downstream. These expansion waves deflected as they passed through the barrel shock generating an expansion fan in the interaction region which turned the freestream around the jet. As the jet turned downstream, separation foci (discussed later) downstream turned the leeward side of the barrel shock away from the surface toward the windward side of the barrel shock. This collapsed the three-dimensional shock on itself, generating a three-dimensional shock reflection. The leeward side of the reflection coalesced with compression waves generated by the downstream separation zone (discussed later). The windward side weakened due to the intersection of the expansion waves that reflected through the windward side of the barrel shock.

This flow structure just described is considerably different from the underexpanded jet issuing into a subsonic freestream. The wave formations in the freestream produced remarkably different flow characteristics. These flow characteristics produced by the presence of these waves are a result of the fundamental inability of pressure disturbances to propagate upstream in supersonic flow (except through the thin subsonic region near the surface). In no better way can these complex characteristics be illustrated than in Fig. 20 where skin friction lines are plotted with surface pressure contours.

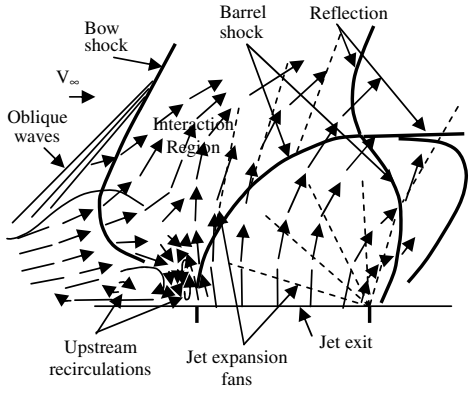

Fig. 19 Sketch of jet and upstream flow structure, $M = 2.0$.

Figure 20 shows skin friction lines in black and surface pressure contours in white with the salient features of the separation topology highlighted. This figure shows four saddle points, one attachment node, and two separation foci with two pairs of global separation lines. The change from a subsonic freestream Mach number to a supersonic freestream Mach number created two pitchfork bifurcations [30]. Downstream, a pitchfork bifurcation changed the two saddle points and attachment node into a single saddle point while another pitchfork bifurcation close to the jet changed the upstream saddle point into two saddle points and one attachment node, classifying this flowfield as a two-dimensional plane cutting a three-dimensional body with four saddle points and three nodes and foci. Furthermore, two other features appeared in the phase portrait. The separation foci moved away from the jet/plate junction and the pair of global separation lines emanating from the new upstream saddle point moved downstream, separated by nearly 7 jet diameters. These separation lines proceeded downstream without ever converging to a node or foci. Without this convergence, a large portion of the plate was covered by the separation zone.

This massive separation around the jet spawned horseshoe vortices, as shown in Fig. 21. Figure 21 shows streamlines coiling up into horseshoe vortices as they follow the dividing surfaces around the jet into the separation zone with skin friction lines in black and surface pressure contours in white. The streamlines wrapped under each other producing a clockwise left-running vortex and the counterclockwise right-running vortex. The emergence of the new saddle point created from the λ-shock structure effectively uncoupled the first set of global separation lines from the horn vortices allowing the horseshoe vortices to form as shown in Fig. 21 and coexist with the horn vortices as shown in Fig. 22.

Figure 22 shows streamlines wrapping around the dividing surfaces emanating from the global separation lines formed between the second saddle point and the two separation foci into horn vortices and streamlines wrapping around the dividing surfaces emanating from the global separation lines originating from the first upstream saddle point into horseshoe vortices. The λ shock altered the flow structure by producing the first upstream saddle point, allowing the horseshoe vortices to develop, forming an upstream attachment node, and producing the transverse pressure gradient necessary to deflect the jet. The alteration of the path of the jet relocated the separation foci downstream moving the horn vortices away from the jet/plate junction and reduced the downstream saddle points to one. This reduction in saddle points prevented the formation of the downstream pair of global separation lines and the formation of the

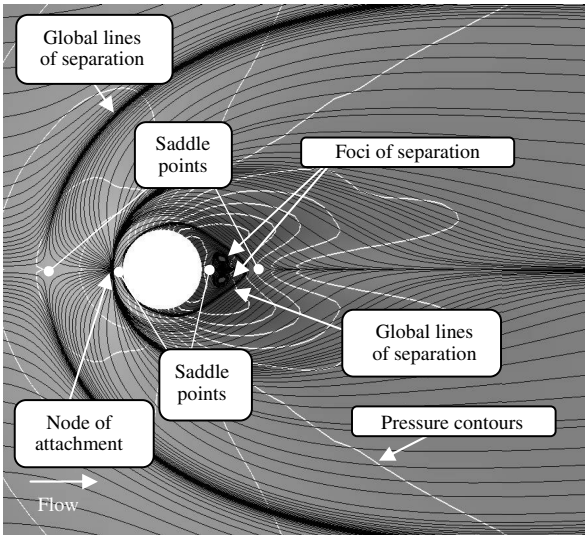

Fig. 20 Skin friction lines around jet, $M = 2.0$.

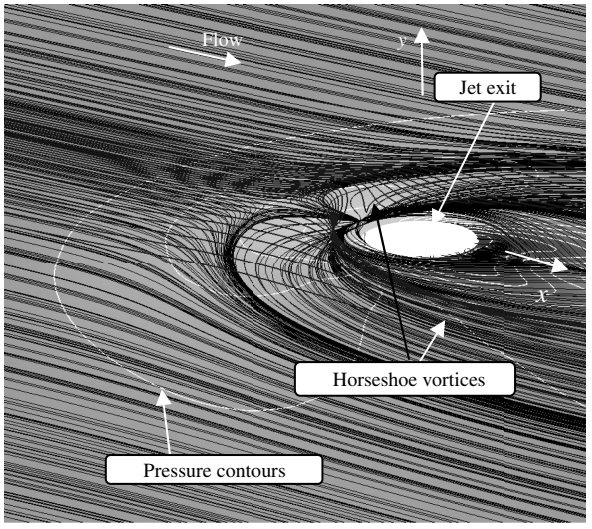

Fig. 21 Horseshoe vortices, $M = 2.0$.

near- and far-field wakes vortices. With no near-field wake vortices and the new pair of global separation lines defining a separation zone much larger than what could be reasonably called "near field," it was viewed as more reasonable to define the near field by the judicious selection of a surface pressure contour as shown in Fig. 23.

Figure 23 shows pressure contours in white with the near-field boundary in bold. The shape of the pressure contours in this simulation was radically different from the subsonic simulation and covered a much larger area. The contours took a more mushroomlike shape with the two-lobe pattern morphing into the stem of the mushroom and the upstream contours resembling the top of the mushroom. The presence of shock and expansion waves altered the shape of the pressure contours, the separation topology, and, ultimately, the surface pressure distributions. Examination of the surface pressure distributions are shown in Figs. 24a and 24b.

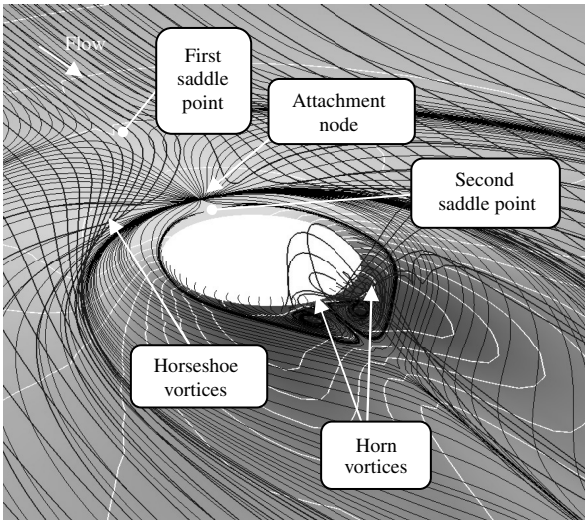

Fig. 22 Horn vortices, $M = 2.0$.

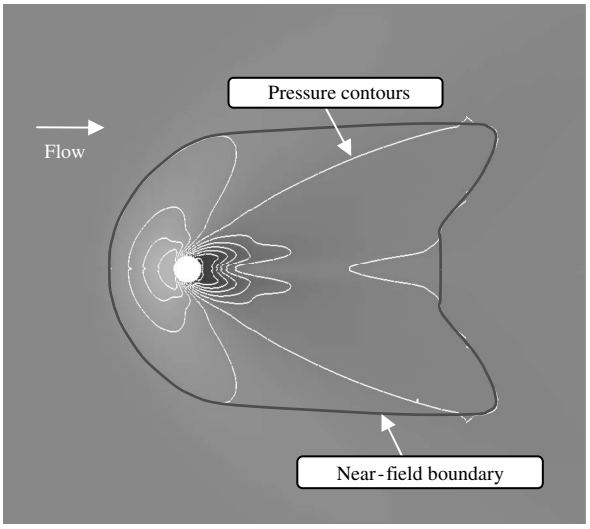

Fig. 23 Skin friction lines around jet, $M = 2.0$.

Table 4 Coefficients for pressure ratio 5

M	PR	$C_{N\text{ji}}$	$C_{m\text{ji}}$	C_T	ε_N	ε_m
0.3	5.0	+1.54e − 3	+7.79e − 4	−1.64e − 3	+0.06	−0.22
2.0	5.0	−5.77e − 5	−2.28e − 5	−3.65e − 5	+2.58	+2.60

Figure 24 shows normalized surface pressure plotted against normalized axial distance upstream and downstream of the jet along the centerline for the PR 5 jet issuing into both subsonic ($M = 0.3$) and supersonic ($M = 2.0$) freestreams with the edge of the jet highlighted for reference. Figure 24a shows the shock waves upstream of the jet elevated the surface pressures 80% above the subsonic case and enlarged the affected area. This marked difference in the upstream region had an amplifying effect on the jet thrust while the downstream surface pressures attenuated the thrust as shown in Fig. 24b where surface pressure downstream of the jet are plotted. The jet expansion waves reduced the surface pressure downstream of the jet by 60% from the subsonic case and enlarged the affected downstream area. Although these distributions show the jet thrust was amplified by the upstream pressure and attenuated by the downstream pressure, the entire surface area had to be integrated to determine the global impact of jet interaction on jet thrust.

Table 4 summarizes the thrust, force, and moment coefficients along with the amplification coefficients for the supersonic and subsonic simulations at jet pressure ratio 5.

At Mach 2.0, JI amplified both the normal force and pitching moment of the jet by more than $2\frac{1}{2}$ times where $\varepsilon_N = +2.59$ and $\varepsilon_M = +2.60$. These coefficients show JI in a supersonic freestream produced an effect opposite to JI in a subsonic freestream where both coefficients were attenuated.

IV. Conclusions

The features for supersonic freestreams were verified, namely, the bow shock, barrel shock, λ shock, Mach disk, jet vortices, and horseshoe vortices. In addition, new flow structures were identified downstream of the jet, namely, horn vortices in the supersonic freestream and horn, near-field wake, and far-field wake vortices in the subsonic freestream. Furthermore, the topological phase portrait experienced two bifurcations when the freestream Mach changed from 0.3 (subsonic) to 2.0 (supersonic). Upstream, singularities in the skin friction lines appeared while downstream singularities disappeared. These bifurcations resulted from the presence of shock and expansion waves which dramatically altered the performance characteristics. In subsonic flow, the jet thrust was nearly nullified by JI while it was more than doubled in the supersonic freestream. The dramatic impact on JI performance characteristic illustrates the

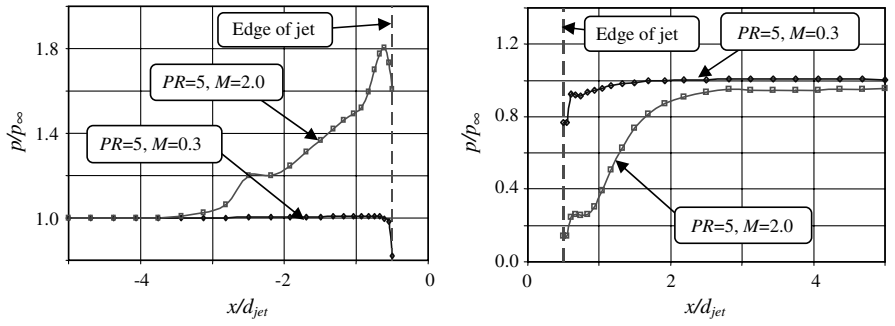

a) Upstream of jet **b) Downstream of jet**

Fig. 24 Streamwise surface pressure distribution along centerline axis, $PR = 5$.

importance of understanding the near-field mean flow structure of transverse jets issuing into a freestream in any regime.

References

[1] Margason, R. J., "Fifty Years of Jet in Cross Flow Research," AGARD, 72nd Fluid Dynamics Panel Meeting, Paper 1, 1993.

[2] Ferrari, C., "Interference Between a Jet Issuing Laterally from a Body and the Enveloping Supersonic Stream," Jet Propulsion Lab. Bumblebee Series, Rept. 286, April 1959.

[3] Spaid, F. W., "A Study of Secondary Injection of Gases into a Supersonic Flow," Ph.D. Dissertation, California Inst. of Technology, Pasadena, CA, 1964.

[4] Spaid, F. W., and Cassel, L. A., "Aerodynamics Interference Induced by Reaction Controls," AGARDograph No. 173, Dec. 1973.

[5] Morkovin, M. V., Pierce, C. A., Jr., and Cravens, C. E., "Interaction of a Side Jet With a Main Stream," Univ. of Michigan Press, Engineering Research Inst. Bulletin No. 35, 1952.

[6] Cubbison, R. W., Anderson, B. H., and Ward, J. J., "Surface Pressure Distributions with a Sonic Jet Normal to Adjacent Flat Surfaces at Mach 2.92 to 6.4," NASA TN-D-580, Feb. 1961.

[7] Fric, T. F., and Roshko, A., "Vortical Structure in the Wake of a Jet," *Journal of Fluid Mechanics*, Vol. 279, 1994, pp. 1–47. doi:10.1017/S0022112094003800

[8] Roger, R. P., and Chan, S. C., "CFD Study of the Flowfield Due to a Supersonic Jet Exiting into a Hypersonic Stream from a Conical Surface," AIAA Paper 93-2926, 1993.

[9] Champigny, P., and Lacau, R. G., "Lateral Jet Control for Tactical Missiles," *Special Course On Missile Aerodynamics*, AGARD-R-804, Paper 3, 1994.

[10] Gruber, M. R., Nejad, A. S., Chen, T. H., and Dutton, J. C., "Mixing and Penetration Studies of Sonic Jets in a Mach 2 Freestream," *Journal of Propulsion and Power*, Vol. 11, No. 2, 1995, pp 315–323. doi:10.2514/3.51427

[11] Dickmann, D. A., "On the Near Field Mean Flow Structure of Transverse Jets Issuing into a Supersonic Freestream," Ph.D. Dissertation, Univ. of Texas at Arlington, Arlington, TX, Dec. 2007.

[12] Smith, B. R., "The *k-kl* Turbulence Model and Wall Layer Model for Compressible Flows," AIAA Paper 90-1483, June 1990.

[13] Dowdy, M. W., and Newton, J. F., "Investigation of Liquid and Gaseous Secondary Injection Phenomena on a Flat Plate with $M = 2.01$ and $M = 4.54$," Jet Propulsion Lab., California Inst. of Technology, TR-32-542, Dec. 1963.

[14] Wilcox, D. C., *Turbulence Modeling for CFD*, 2nd ed., DCW Industries, La Cañada, CA, 1998.

[15] Van Leer, B., "A New Approach to Numerical Gas Dynamics," *Computing in Physics and Astrophysics*, Max-Planck-Institut fur Plasma Physik, Garchung, Germany, 1976.

[16] Roe, P. L., "Approximate Riemann Solvers, Parameter Vectors and Differencing Schemes," *Journal of Computational Physics*, Vol. 43, No. 2, 1981, pp. 357–372. doi:10.1016/0021-9991(81)90128-5

[17] Sweby, P. K., "High Resolution Schemes Using Flux Limiters for Hyperbolic Conservative Laws," *SIAM Journal on Numerical Analysis*, Vol. 21, No. 5, 1984, pp. 995–1101. doi:10.1137/0721062

[18] Stone, H. L., "Iterative Solution of Implicit Approximations of Multidimensional Partial Differential Equations," *SIAM Journal on Numerical Analysis*, Vol. 5, No. 3, 1968, pp. 530–558. doi:10.1137/0705044

[19] Shutts, W. H., Hartwig, W. H., and Weiler, J. E., "Final Report on Turbulent Boundary Layer and Skin Friction Measurements on a Smooth, Thermally Insulated Flat Plate at Supersonic Speeds," Defense Research Lab., Univ. of Texas, Rept. 364, 1955.

[20] Mabey, D. G., Meier, H. U., and Sawyer, W. G., "Experimental and Theoretical Studies of the Boundary Layer on a Flat Plate at Mach Numbers from 2.5 to 4.5," Royal Aircraft Establishment TR 74127, 1974.

[21] Fernholz, H. H., and Finley, P. J., "A Critical Compilation of Compressible Turbulent Boundary Layer Data," AGARDograph, No. 223, June 1977.

[22] Lu, F. K., "Fin Generated Shock-Wave Boundary-Layer Interactions," Ph.D. Dissertation, Pennsylvania State Univ., University Park, PA, May 1988.

[23] White, F. W., *Fluid Mechanics*, McGraw–Hill, New York, 1979.

[24] Hopkins, E. J., and Inouye, M., "An Evaluation of Theories for Predicting Turbulent Skin Friction and Heat Transfer on Flat Plates at Supersonic and Hypersonic Mach Number," *AIAA Journal*, Vol. 9, No. 6, 1971, pp. 993–1003. doi:10.2514/3.6323

[25] Lighthill, M. J., "Attachment and Separation in Three-Dimensional Flow," *Laminar Boundary Layers*, Vol. 2, Sec. 2.6, L. Rosenhead (ed.), Oxford Univ. Press, Oxford, England, U.K., 1963, pp. 72–82.

[26] Tobak, M., and Peake, D. J., "Topology of Three-Dimensional Separated Flow," *Annual Review of Fluid Mechanics*, Vol. 14, Jan. 1982, pp. 61–85. doi:10.1146/annurev.fl.14.010182.000425

[27] Legendre, R., "Séparation de l'Écoulement Laminaire Tridimensionnel," *Recherche Aéronautique*, Vol. 53, 1956, pp. 3–8.

[28] Davey, A., "Boundary Layer Flow at a Saddle Point of Attachment," *Journal of Fluid Mechanics*, Vol. 10, No. 4, 1961, pp. 593–610. doi:10.1017/S0022112061000391

[29] Shapiro, A. H., *The Dynamics and Thermodynamics of Compressible Fluid Flow*, Vol 2, Wiley, New York, 1954.

[30] Chapman, G. T., "Topological Classification of Flow Separation on Three-Dimensional Bodies," AIAA Paper 86-0485, 1986.

R. Cummings
Associate Editor